Computers & Intelligent Decision Applications

Journal homepage: www.cidai-journal.org
eISSN: 3123-125X

Intelligent Computational Framework for Thermo-Vibrational Response and Critical Speed Prediction in Rotating Functionally Graded Annular Disks

Hüseyin Fırat Kayiran[1,*]

[1] Presidency of the Agriculture and Rural Development Support Institution, Mersin Provincial Coordination Office, Mersin, Turkey

ARTICLE INFO

Article history:
Received 4 June 2026
Received in revised form 11 July 2026
Accepted 8 August 2026
Available online 11 September 2026

Keywords:
Machine Learning; Computational Intelligence; Functionally Graded Materials; Thermo-vibrational Analysis; Critical Speed

ABSTRACT

This study presents a numerical and machine-learning-assisted framework for investigating the thermo-vibration characteristics of a rotating functionally graded Al–SiC annular disk. The aluminium and silicon-carbide volume fractions vary continuously in the radial direction according to a power-law distribution. The governing thermoelastic and transverse-vibration equations are solved using the Chebyshev spectral collocation method. The formulation incorporates a non-uniform radial temperature field, radially graded and temperature-dependent material properties, centrifugal prestress, thermal membrane forces, and rotation-induced splitting of travelling-wave frequencies. Numerical convergence is examined by progressively increasing the collocation order. The generated database is used to train multilayer perceptron, gradient-boosting, and Gaussian-process regression models. For the baseline disk, the first natural frequency in the rotating frame is 1500.23 Hz, while the forward- and backward-travelling wave frequencies are 1579.81 and 1420.65 Hz, respectively. Gradient boosting provides the best overall test performance (R^2 = 0.8661), whereas critical-speed prediction remains less accurate (R^2 = 0.5770). The framework provides an efficient computational tool for thermo-vibrational assessment and preliminary design of functionally graded rotating annular disks.

1. Introduction

Rotating disks are essential structural components in gas turbines, flywheels, energy-storage systems, automotive brakes, centrifugal machinery, and various aerospace applications. During operation, these components are subjected to centrifugal forces that generate substantial radial and circumferential stresses. When rotation is accompanied by a non-uniform temperature field, constrained thermal expansion interacts with the centrifugal response and produces a complex thermo-mechanical stress state. Accurate prediction of this coupled behavior is therefore important for limiting deformation, preventing local yielding, and improving the operational reliability of high-speed rotating systems [1, 2].

Conventional rotating disks are generally manufactured from homogeneous metallic materials. Although these materials provide predictable mechanical performance, their effectiveness may be

* *Corresponding author.*
E-mail address: huseyinfiratkayiran@gmail.com

limited under severe combinations of high rotational speed, elevated temperature, and steep radial temperature gradients. Functionally graded materials offer an alternative solution because their mechanical and thermal properties can be varied continuously within the component. This gradual transition reduces abrupt property discontinuities and may alleviate the interfacial stress concentrations commonly encountered in traditional multilayer structures [3, 4].

Several researchers have investigated the elastic response of rotating functionally graded disks. Bayat *et al.,* [5] examined annular and solid disks with radially varying thickness and demonstrated that the selected material distribution significantly influences both the stress field and radial displacement. Asghari and Ghafoori [6] subsequently developed a three-dimensional elasticity solution to evaluate the behavior of functionally graded rotating disks without relying entirely on simplified two-dimensional assumptions. Çallıoğlu *et al.,* [7] combined an analytical formulation with finite-element simulations and showed that the material-gradient parameter can be employed to modify the circumferential-stress distribution and reduce critical radial stresses.

The influence of geometric non-uniformity has also received considerable attention. Zafarmand and Hassani [8] studied two-dimensional rotating thick disks with different thickness profiles and radially graded material properties. Their results indicated that the simultaneous control of disk thickness and material gradation provides an effective means of tailoring the structural response. Additional analytical and numerical investigations have shown that the boundary conditions, thickness variation, density distribution, and rotational velocity determine not only the magnitudes of the stresses but also the radial locations at which their critical values occur [9, 10].

Thermal loading introduces an additional design concern for high-speed rotating structures. Hosseini Kordkheili and Naghdabadi [11] examined the thermoelastic behavior of a functionally graded rotating disk and demonstrated that thermally induced stresses may become comparable to mechanically induced stresses when a pronounced temperature gradient is present. Dai and Dai [12] investigated a rotating hollow disk with variable thickness and angular speed, emphasizing the coupled influences of thermal loading, geometric variation, and material gradation. Carrera *et al.,* [13] developed a one-dimensional finite-element formulation capable of reproducing the three-dimensional thermoelastic response of rotating disks with arbitrary profiles. Analytical solutions based on coupled thermoelasticity have also been proposed for rotating disks subjected to thermal, mechanical, and shock-type loads [14, 15]. Material anisotropy further modifies the behavior of rotating disks. Polar orthotropic formulations are particularly relevant to fiber-reinforced composites because their elastic properties differ in the radial and circumferential directions. Peng and Li [16] demonstrated that the orthotropy ratio and material-gradient index strongly affect the radial and circumferential stress distributions. Jalali and Jalali [17] extended this subject to variable-thickness functionally graded polar orthotropic disks exposed to combined rotational and thermal loading. Their finite-difference results indicated that temperature variation, gradation index, material orthotropy, and support conditions may cause considerable changes in radial stress and displacement. The thermo-mechanical response of rotating disks is also important in automotive braking systems. Frictional work generated during braking is transformed into heat at the pad–rotor interface, producing rapidly varying temperatures and high local thermal stresses. These stresses may contribute to distortion, surface cracking, thermal fatigue, and reduced braking efficiency. Numerical and experimental investigations have consequently focused on transient temperature distributions and coupled thermal–structural behavior in both solid and ventilated brake disks [18, 19]. Jiregna and Lemu [20], for example, compared analytical and finite-element predictions and reported that high temperatures and thermal stresses develop near the rubbing surfaces, where the temperature gradients are most pronounced. At the broader transportation-system level, Farooq *et al.,* [21] used a spherical fuzzy analytic hierarchy process to prioritize factors shaping drivers' perceived road-safety risk. Although that study addressed infrastructure and human perception rather than component mechanics, it reinforces the value of intelligent, multi-factor assessment; the present work complements this system-level perspective through physics-based and data-driven prediction of a safety-critical rotating component.

Recent studies have increasingly combined thermoelastic mechanics with artificial intelligence. Kayiran [22] accelerated thermoelastic-stress prediction in hybrid SiC–Ti6Al4V components using machine learning. Explainable physics-informed deep learning was subsequently applied to the thermoelastic analysis of rotating Ti–6Al–4V disks [23], and physics-informed machine learning was used to predict thermomechanical stresses in rotating carbon–aramid hybrid composites [24]. Together, these developments support the integration of physics-based solvers and data-driven surrogates adopted in the present study.

2. Materials and Methods

2.1 Geometry and Material Gradation

Numerical analyses were conducted on an annular disk with inner and outer radii of 50 mm and 90 mm, respectively. The parametric dataset was constructed considering temperature differences (delta T = 40, 80, 120, 160, 180, and 200 deg C), rotational speeds (Omega = 50 to 1500 rad/s), material-gradient indices (k = 0.15 to 8.0), radius ratios (a/b = 0.25 to 0.75), thickness ratios (h/b = 0.012 to 0.050), and circumferential wave numbers (n = 1, 2, 3, 4). The geometry and principal dimensions of the annular disk are shown in Figure 1.

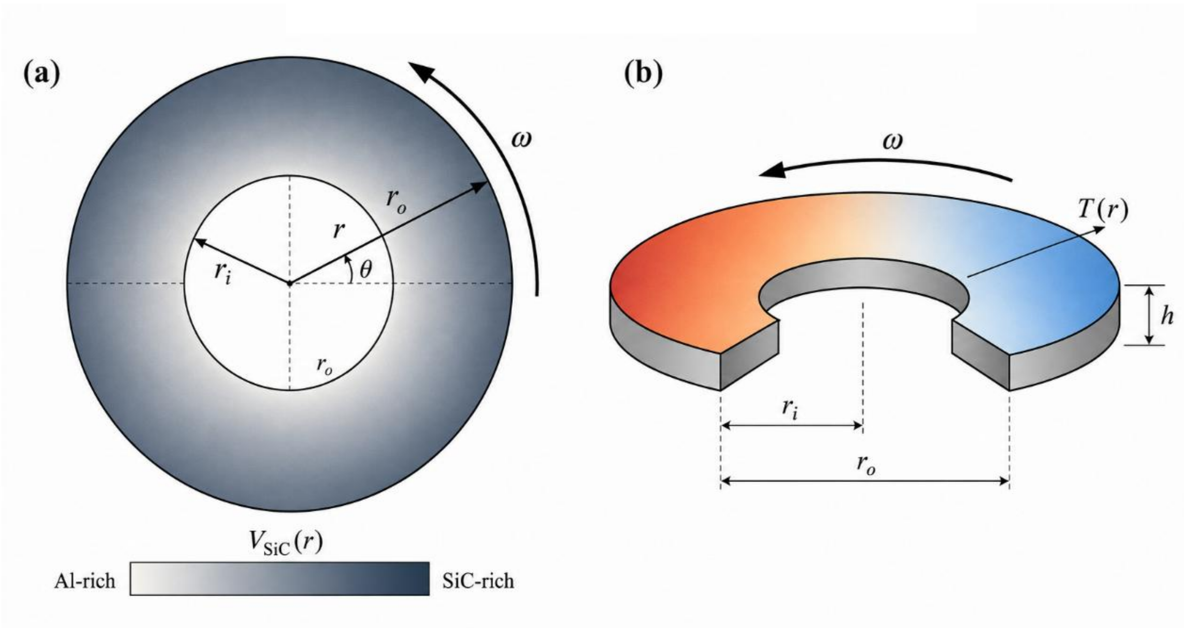

Fig. 1. Geometry of the rotating FGM Al–SiC annular disk

The hollow disk has an inner radius of 50 mm, an outer radius of 90 mm, and a uniform thickness of 2 mm. The thickness-to-outer-diameter ratio is approximately 0.011. Therefore, the disk was modeled under plane-stress conditions.

The mechanical properties of the disc material are given below in Table 1.

Table 1
Temperature-independent reference material properties of Al and SiC [25]

Material Property	Aluminium (Al)	Silicon Carbide (SiC)
Young's Modulus (E)	70 GPa	380 GPa
Density	2700 kg/m³	3100 kg/m³
Poisson's Ratio	0.30	0.17
Thermal Expansion Coefficient	23 *10-6 1/K	4.0 10-61/K

2.2 Analytical Formulation

A thin functionally graded annular disk with inner radius a, outer radius b, and uniform thickness h is considered. The disk rotates about its central axis at a constant angular velocity Ω. The material is assumed to be locally isotropic, while its composition varies continuously along the radial direction. Small deformations, linear elastic material behavior, and the classical Kirchhoff–Love thin-plate assumptions are adopted [26]. The disk is composed of aluminium and silicon carbide. The SiC volume fraction is described by the following radial power-law distribution:

$$V_{\mathrm{SiC}}(r) = \left(\frac{r-a}{b-a}\right)^n \tag{1}$$

$$V_{\mathrm{Al}}(r) = 1 - V_{\mathrm{SiC}}(r) \tag{2}$$

$$\mathrm{P}(\mathrm{r},\mathrm{T}) = \mathrm{P_A l(T) V_A l(r)} + \mathrm{P_S iC(T) V_S iC(r)} \tag{3}$$

In the present implementation, Young's modulus and the coefficient of thermal expansion are treated as temperature-dependent. Density, Poisson's ratio, and thermal conductivity vary with the local Al–SiC composition but are evaluated using their reference constituent values. The temperatures prescribed at the inner and outer edges are:

$$T(a) = T_i, \qquad T(b) = T_o \tag{4}$$

The applied temperature difference is defined as:

$$\Delta T = T_o - T_i \tag{5}$$

When the variation in thermal conductivity is neglected, integration of the steady radial heat-conduction equation gives the following logarithmic radial temperature distribution:

$$T(r) = T_i + (T_o - T_i)\frac{\ln(r/a)}{\ln(b/a)} \tag{6}$$

The prescribed logarithmic field corresponds to steady axisymmetric heat conduction in an annular domain under the assumption of constant effective thermal conductivity. Equation (6) satisfies both temperature boundary conditions and represents the steady-state temperature field in the annular geometry.

2.3 Thermo-Centrifugal Prestress

The combined effects of the temperature field and rotational motion generate an axisymmetric prestress state before transverse vibration occurs. The radial equilibrium equation, including the centrifugal body force, is expressed as:

$$\frac{d\sigma_r^0}{dr} + \frac{\sigma_r^0 - \sigma_\theta^0}{r} + \rho(r,T)\Omega^2 r = 0 \tag{7}$$

$$\begin{bmatrix}\sigma_r^0\\ \sigma_\theta^0\end{bmatrix} = \frac{E(r,T)}{1-\nu^{2(r,T)}}\begin{bmatrix}1 & \backslash nu(r,T)\\ \nu(r,T) & 1\end{bmatrix}\left[\begin{bmatrix}\frac{du_0}{dr}\\ \frac{u_0}{r}\end{bmatrix} - \alpha(r,T)\big(T(r) - T_{ref}\big)\begin{bmatrix}1\\1\end{bmatrix}\right] \tag{8}$$

In Eq. (8), u_0 is the radial displacement in the thermo-mechanically prestressed configuration, and Tref is the stress-free reference temperature. The radial and circumferential membrane-force resultants are:

$$N_r^0(r) = h\sigma_r^0(r), \qquad N_\theta^0(r) = h\sigma_\theta^0(r) \tag{9}$$

The radially varying flexural rigidity of the functionally graded disk is defined as:

$$D(r,T) = \frac{E(r,T)h^3}{12[1-\nu^2(r,T)]} \tag{10}$$

The inner edge is assumed to be radially constrained, while the outer edge is traction-free. The in-plane boundary conditions are therefore:

$$u_0(a) = 0, \qquad \sigma_r^0(b) = 0 \tag{11}$$

2.4 Transverse Vibration Model

The transverse displacement is represented by a harmonic travelling-wave solution:

$$w(r,\theta,t) = W(r)e^{i(m\theta-\omega t)} \tag{12}$$

Here, W(r) is the radial mode-shape function, m is the circumferential wave number, and ω is the natural angular frequency. Because the disk rotates, the acceleration of a material point is determined using the convective derivative:

$$\frac{D^2w}{Dt^2} = \frac{\partial^2 w}{\partial t^2} + 2\Omega\frac{\partial^2 w}{\partial t\,\partial\theta} + \Omega^2\frac{\partial^2 w}{\partial\theta^2} \tag{13}$$

The second term in Eq. (13) represents the gyroscopic contribution, whereas the final term represents the spin-dependent contribution to the dynamic response. The linearized transverse vibration equation of the thermo-mechanically prestressed disk is written in compact operator form as:

$$\mathcal{L}_{\mathcal{B}}(w) - \frac{1}{r}\frac{\partial}{\partial r}\left(rN_r^0\frac{\partial w}{\partial r}\right) - \frac{N_\theta^0}{r^2}\frac{\partial^2 w}{\partial\theta^2} + \rho(r,T)h\frac{D^2w}{Dt^2} = 0 \tag{14}$$

In Eq. (14), $\mathcal{L}$B represents the variable-coefficient bending operator formed using the local flexural rigidity D(r,T). The second and third terms account for the geometric-stiffness contributions of the thermal and centrifugal prestresses. The inner edge of the disk is assumed to be clamped, while its outer edge is free. The transverse boundary conditions are:,

$$W(a) = 0, \qquad \left.\frac{dW}{dr}\right|_{r=a} = 0, \qquad M_r(b) = 0, \qquad V_r(b) = 0 \tag{15}$$

Here, Mr and Vr denote the radial bending moment and effective transverse shear force, respectively.

2.5 Chebyshev Spectral Collocation Method

The Chebyshev spectral collocation method is employed to obtain a high-accuracy numerical solution of the governing thermo-vibration equations. Unlike low-order discretization techniques, spectral differentiation represents the spatial derivatives through global interpolation polynomials constructed at non-uniform Chebyshev–Gauss–Lobatto points. This approach generally provides rapid convergence for sufficiently smooth solutions and enables the governing differential equations and boundary conditions to be converted directly into a matrix eigenvalue problem [27]. The physical radial interval is mapped onto the computational domain x ∈ [−1, 1]. The material properties, temperature field, thermo-centrifugal prestresses, and differential operators are evaluated at the collocation points. The mechanical boundary conditions are subsequently imposed by replacing the corresponding rows of the discretized system. Natural frequencies and mode shapes are then determined from the resulting quadratic eigenvalue problem. The physical radial interval is transformed into the Chebyshev computational domain. The Chebyshev–Gauss–Lobatto points and their corresponding physical radial coordinates are defined as:

$$x_j = \cos\left(\frac{j\pi}{N}\right), \qquad r_j = \frac{a+b}{2} + \frac{b-a}{2}x_j, \qquad j = 0,1,\dots,N \tag{16}$$

The radial differentiation matrices are obtained from:

$$D_r^{(p)} = \left(\frac{2}{b-a}\right)^p \boldsymbol{D}_{\boldsymbol{x}}^{(\boldsymbol{p})}, \qquad p = 1,2,3,4 \tag{17}$$

The material properties, temperature field, prestresses, and governing differential operators are evaluated at the Chebyshev collocation points. After imposing the mechanical boundary conditions, the continuous vibration problem is converted into the following quadratic eigenvalue problem:

$$[K_B + K_G - m^2\Omega^{2M} + 2m\Omega\omega M - \omega^{2M}]q = 0 \tag{18}$$

Here, K_B is the variable-flexural-rigidity matrix, K_G is the geometric-stiffness matrix associated with the combined thermal and centrifugal prestresses, and M is the mass matrix. The terms $-m^2\Omega^2M$ and $2m\Omega\omega M$ originate from the spin-dependent and gyroscopic components of the convective acceleration, respectively. The expanded and compact formulations are algebraically equivalent. In the numerical implementation, the rotating-frame modes are first obtained, after which the corresponding quadratic travelling-wave equation is solved for each mode. In Eq. (18), KB is the bending-stiffness matrix, KG is the thermo-centrifugal geometric- stiffness matrix, KΩ is the spin-dependent stiffness matrix, CG is the gyroscopic matrix, M is the mass matrix, and q is the vector of discretized modal amplitudes. The natural frequency in hertz is obtained from:

$$f = \frac{\omega}{2\pi} \tag{19}$$

For each non-axisymmetric mode with m ≥ 1, disk rotation removes the frequency degeneracy and separates the modal frequency into forward- and backward-travelling wave branches. The stationary-frame frequencies are expressed as:

$$\omega_m^{\mathrm{F}} = \omega_m^{\mathrm{R}} + m\Omega, \qquad \omega_m^{\mathrm{B}} = |\omega_m^{\mathrm{R}} - m\Omega| \tag{20}$$

These expressions are the two travelling-wave solutions of the modal-reduced quadratic eigenvalue equation. Here, ωm^{R} is the modal frequency measured in the rotating reference frame, while ωm^{f} and ωm^{B} are the forward- and backward-travelling wave frequencies, respectively. The critical rotational speed is determined from the backward-wave condition:

$$\omega_m^{\mathrm{R}}(\Omega_{\mathrm{cr}}) - m\Omega_{\mathrm{cr}} = 0 \tag{21}$$

The first critical rotational speed is located using a bracketed root-search procedure followed by Brent's method. Parameter combinations for which the backward-wave branch does not reach zero within the adaptively expanded search interval are classified as non-crossing cases and are excluded from the critical-speed machine-learning dataset.

Accordingly, the critical speeds are identified from the intersections between the modal-frequency branches and the corresponding excitation lines in the Campbell diagram. The radius ratio and thickness ratio are defined as:

$$\eta = \frac{a}{b}, \qquad \delta = \frac{h}{b} \tag{22}$$

The dimensionless natural frequency and rotational speed are defined as:

$$\overline{\omega} = \omega b^2 \sqrt{\frac{\rho_{\mathrm{Al}} h}{D_{\mathrm{Al}}}} \tag{23}$$

$$\overline{\Omega} = \Omega b^2 \sqrt{\frac{\rho_{\mathrm{Al}} h}{D_{\mathrm{Al}}}} \tag{24}$$

The reference flexural rigidity of aluminium is:

$$D_{\mathrm{Al}} = \frac{E_{\mathrm{Al}} h^3}{12\left(1-\nu_{\mathrm{Al}}^2\right)} \tag{25}$$

These dimensionless quantities are employed to investigate the effects of material gradation, temperature difference, rotational speed, radius ratio, and thickness ratio independently of the selected system of units.

3. Machine-Learning-Assisted Prediction

The numerical solutions obtained using the Chebyshev spectral model are used to construct a supervised-learning database. The input variables include temperature difference, rotational speed, material-gradient index, radius ratio, thickness ratio, and circumferential wave number, while the target variables comprise natural frequencies, forward- and backward-travelling wave frequencies, and critical rotational speeds. A multilayer perceptron (MLP) is employed to capture nonlinear relationships between the thermo-mechanical inputs and modal outputs [28]. Gradient-boosting regression (GBR) is used to model complex nonlinear interactions through sequential error correction [29], whereas Gaussian-process regression (GPR) provides a probabilistic alternative that also enables predictive-uncertainty estimation [30]. The three models are evaluated using an independent test dataset and cross-validation based on R^2, RMSE, and MAE. Input standardization and hyperparameter selection are performed using only the training data to prevent information leakage.

Feature-importance analysis is further performed to identify the relative effects of the temperature difference, rotational speed, material-gradient index, radius ratio, thickness ratio, and circumferential wave number. Permutation feature importance is employed to quantify the sensitivity of the best-performing regression model to each input variable. For a given feature, its values in the independent test dataset are randomly permuted while the remaining variables are retained. The resulting decrease in predictive performance is interpreted as the importance of that feature. This procedure is repeated several times to reduce the influence of random permutation variability. The numerical solutions obtained from the Chebyshev spectral model are used to construct the machine-learning database. The input variables include the temperature difference, rotational speed, material-gradient index, radius ratio, thickness ratio, and circumferential wave number. The machine-learning input vector is:

$$x = [\Delta T, \Omega, n, \eta, \delta, m]^{\mathrm{T}} \tag{26}$$

The output vector includes the natural frequency, forward-wave frequency, backward-wave frequency, and critical rotational speed:

$$y = [\omega_m, \omega_m^{\mathrm{F}}, \omega_m^{\mathrm{B}}, \Omega_{\mathrm{cr}}]^{\mathrm{T}} \tag{27}$$

Multilayer perceptron, gradient-boosting, and Gaussian-process regression models are trained using the generated numerical database. Their prediction performances are assessed using an independent test dataset and cross-validation. The coefficient of determination is calculated from:

$$R^2 = 1 - \frac{\sum_{i=1}^{N}(y_i - \hat{y}_i)^2}{\sum_{i=1}^{N}(y_i - \bar{y})^2} \tag{28}$$

The root-mean-square error and mean absolute error are:

$$\mathrm{RMSE} = \sqrt{\frac{1}{N}\sum_{i=1}^{N}(y_i - \hat{y}_i)^2}, \qquad \mathrm{MAE} = \frac{1}{N}\sum_{i=1}^{N}|y_i - \hat{y}_i| \tag{29}$$

Here, yi represents the reference value calculated by the Chebyshev spectral method, and ŷi is the corresponding machine-learning prediction. All preprocessing parameters and model hyperparameters are determined using only the training dataset to prevent information leakage from the independent test data.

4. Results and Discussion

In this section, the coupled thermo-mechanical, dynamic, and machine-learning-assisted prediction results of the rotating functionally graded Al–SiC annular disk are presented and discussed. First, the baseline thermo-mechanical response—including the radial temperature distribution, thermo-centrifugal prestresses, radial mode shapes, and Campbell diagram branches—is analyzed to characterize the core physical behavior of the system.

The quantitative performances of the machine-learning models for the modal-frequency responses and critical rotational speed are presented separately in Tables 2 and 3.

Table 2
Performance comparison of the machine-learning models for modal-frequency prediction

Model	Rotating-frame R^2	RMSE	MAE	Forward-wave R^2	RMSE	MAE	Backward-wave R^2	RMSE	MAE
MLP	0.8516	0.1474	0.1078	0.8559	0.1541	0.1139	0.8511	0.1498	0.1077
Gradient Boosting (GB)	0.8661	0.1397	0.1020	0.8757	0.1477	0.1072	0.8746	0.1441	0.1046
Gaussian Process Regression (GPR)	0.8352	0.1547	0.1145	0.8366	0.1636	0.1204	0.8365	0.1568	0.1142

Table 3
Performance comparison of the machine-learning models for critical rotational speed prediction

Model	R^2	RMSE	MAE
MLP	0.5562	0.1358	0.1047
Gradient Boosting (GB)	0.5770	0.1318	0.1031
Gaussian Process Regression (GPR)	0.5293	0.1396	0.1069

The coupled thermo-mechanical, dynamic, and machine-learning-assisted results are presented in this section. The baseline thermo-dynamic response is first examined through the temperature, prestress, modal, and Campbell-diagram characteristics. The predictive capabilities of the MLP, Gradient Boosting, and Gaussian Process Regression models are subsequently evaluated using independent test data. Model performance is compared using R^2, RMSE, and MAE, followed by residual, correlation, and permutation feature-importance analyses. Finally, the neural-network architecture and the proposed intelligent computational framework are presented to demonstrate the integration of high-fidelity spectral computation with data-driven surrogate prediction. As shown in Tables 2 and 3, Gradient Boosting consistently provided the best predictive performance among the investigated models. For the modal-frequency responses, the model achieved R^2 values between 0.8661 and 0.8757. In contrast, the prediction of critical rotational speed was more challenging, with a maximum R^2 of 0.5770. These results indicate that the machine-learning surrogate is more suitable for rapid prediction of modal-frequency responses, whereas the Chebyshev spectral solution should be retained for high-accuracy critical-speed assessment. Subsequently, the predictive performance and residual distributions of the regression models (Gradient Boosting, Gaussian Process, and MLP) are evaluated across the parametric database. Finally, the relative importance of the geometric, thermal, dynamic, and material parameters is quantified using permutation feature importance analysis. The baseline thermo-dynamic response is presented in Figure 2.

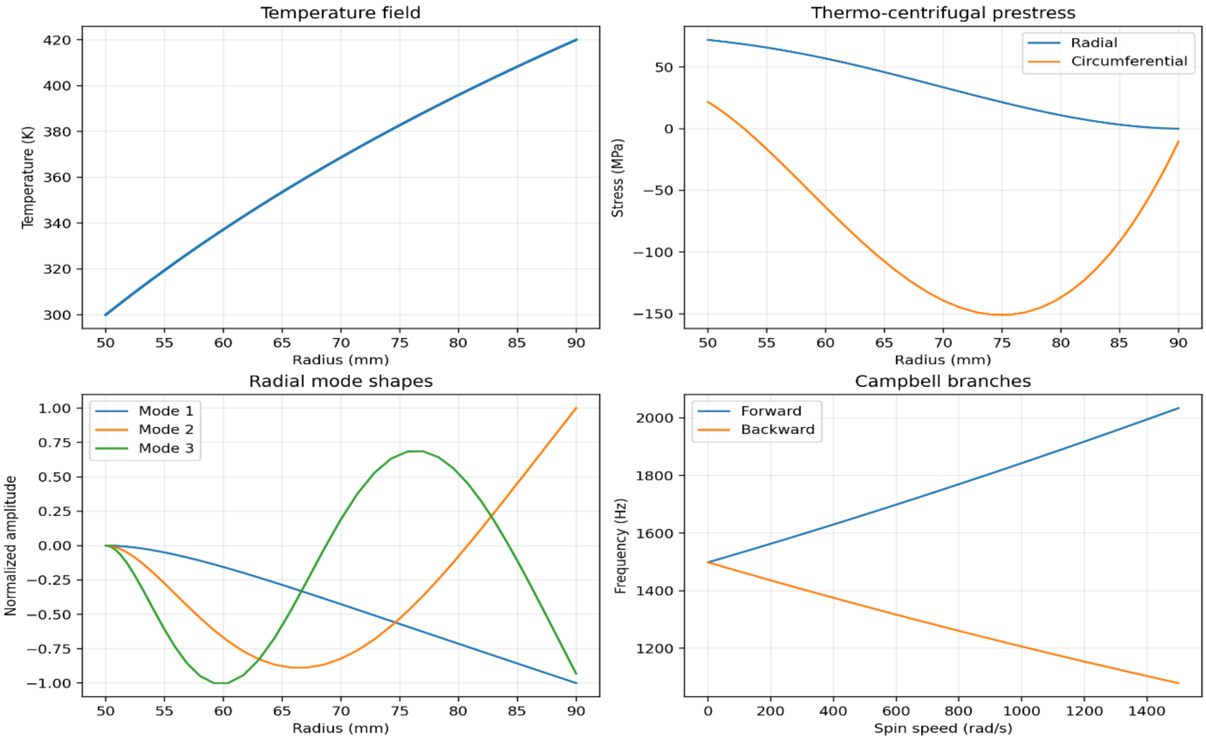

Fig. 2. Thermal, stress, modal, and Campbell responses of the baseline disk

For additional spatial visualization of the baseline thermo-mechanical response, the axisymmetric radial solutions were mapped onto the annular-disk surface. Figure 3 shows the resulting two-dimensional temperature and circumferential thermo-centrifugal prestress contours under the baseline conditions.

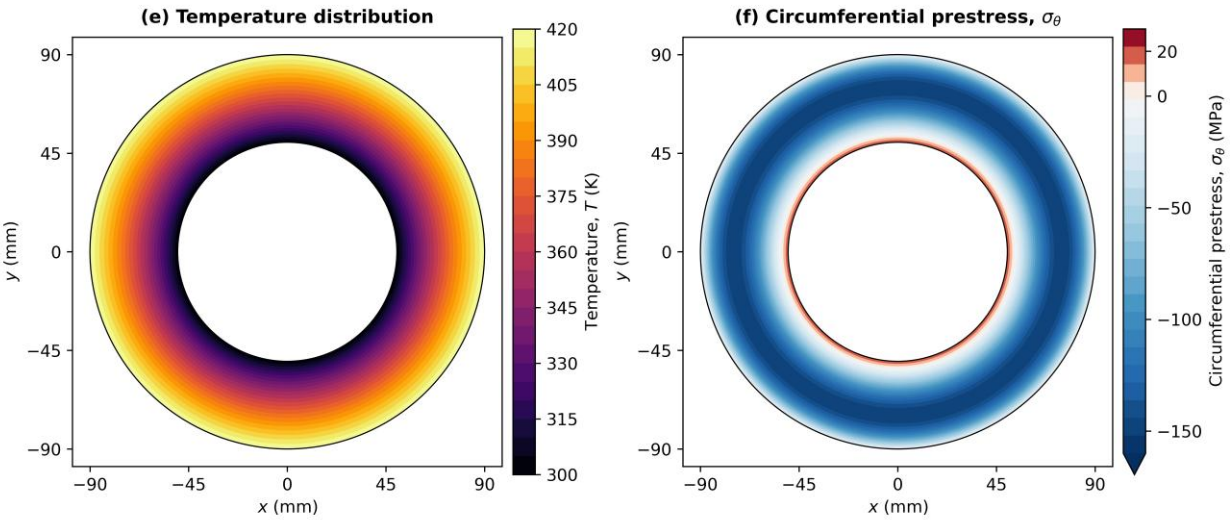

Fig. 3. Two-dimensional contour maps of the baseline FGM Al-SiC annular disk: (a) temperature distribution and (b) circumferential thermo-centrifugal prestress. The contours were reconstructed from the axisymmetric radial solutions under the baseline conditions reported in the manuscript

The agreement between the numerical and predicted values is shown in Figure 4.

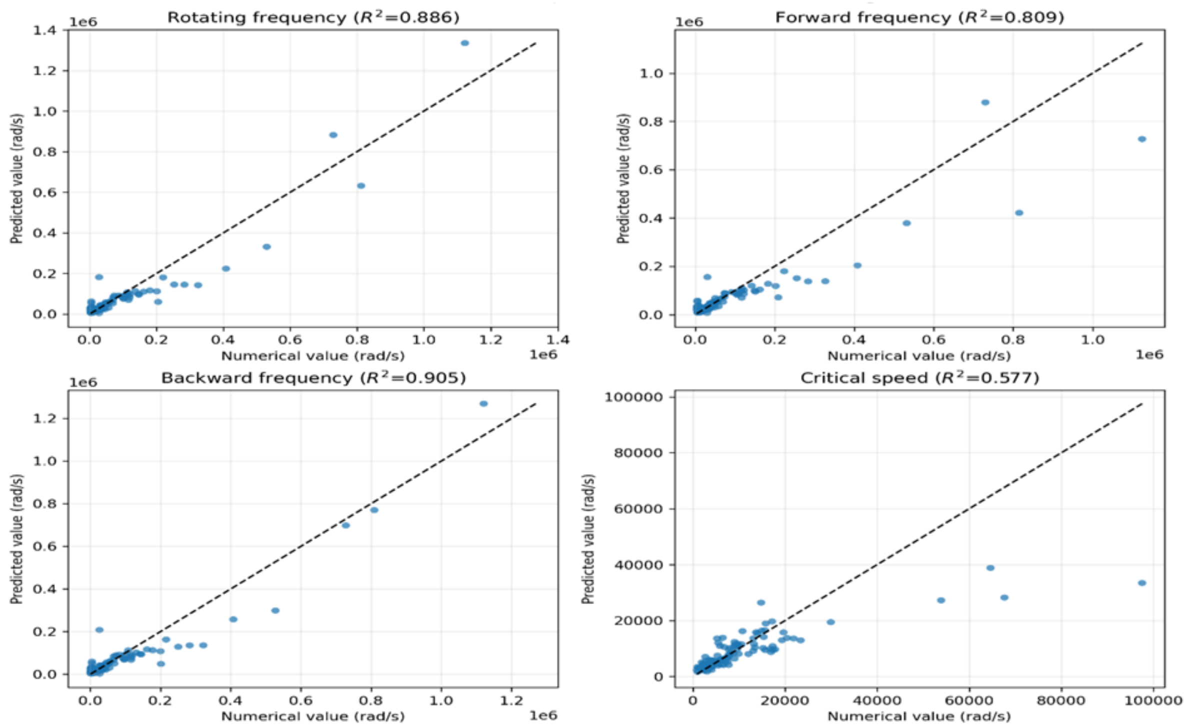

Fig. 4. Numerical and predicted responses obtained using the best-performing model

To explore the linear dependencies among the thermo-mechanical parameters and the resulting dynamical outputs, a bivariate correlation matrix was constructed. The linear statistical relationships and mutual dependencies among the input and output variables are illustrated in Figure 5.

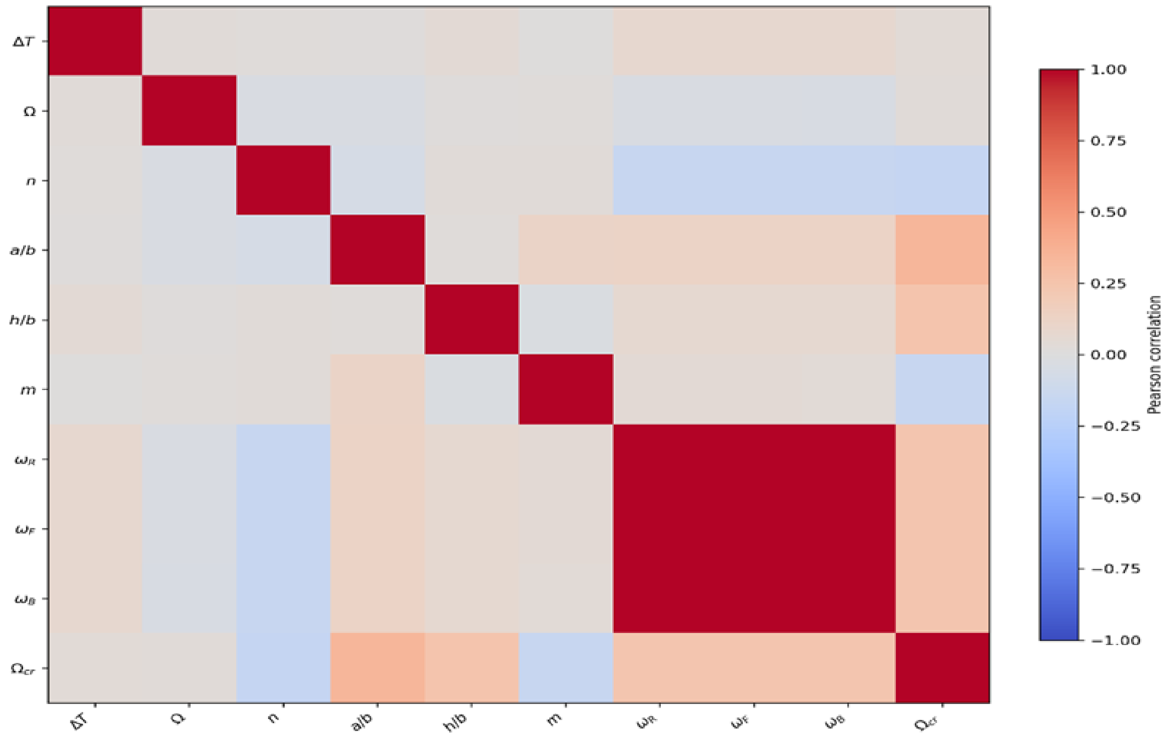

Fig. 5. Correlation map of the numerical input and output variables

The sensitivity of the dynamic predictions to individual parametric variations was assessed using a permutation feature importance scheme. The relative contributions and overall importance rankings of the input parameters in governing the target outputs are displayed in Figure 6. Permutation-based importance of the input parameters

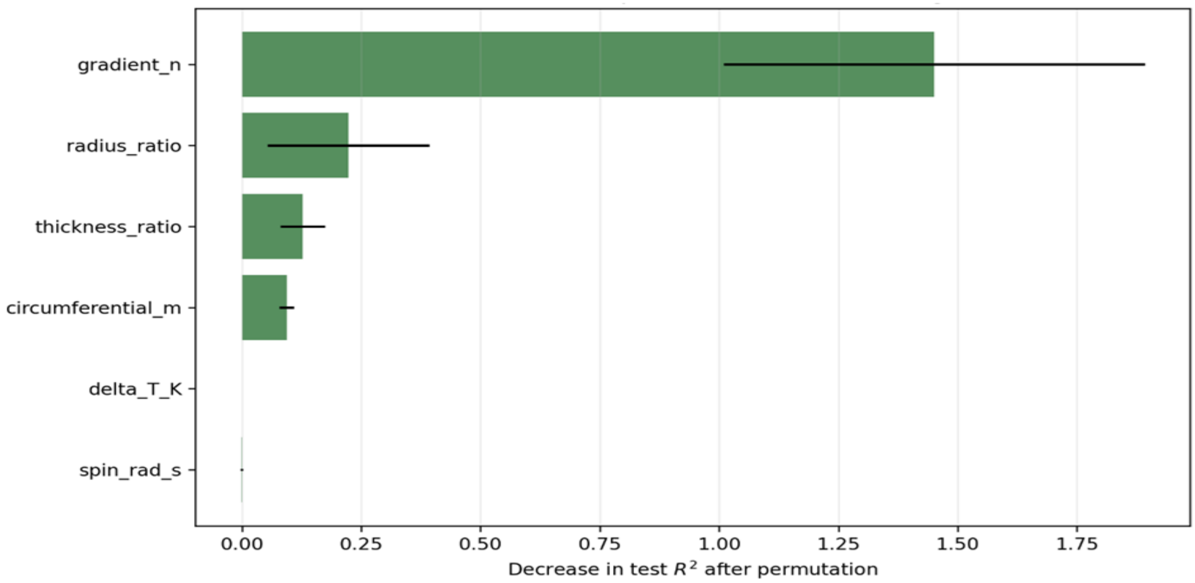

Fig. 6. Permutation-based importance of the input parameters

To compare the overall generalization capabilities of the candidate surrogate models, test metrics including R^2, RMSE, and MAE were evaluated. The comparative performance metrics of the Gradient Boosting, Gaussian Process, and MLP models across the independent test dataset are summarized in Figure 7.

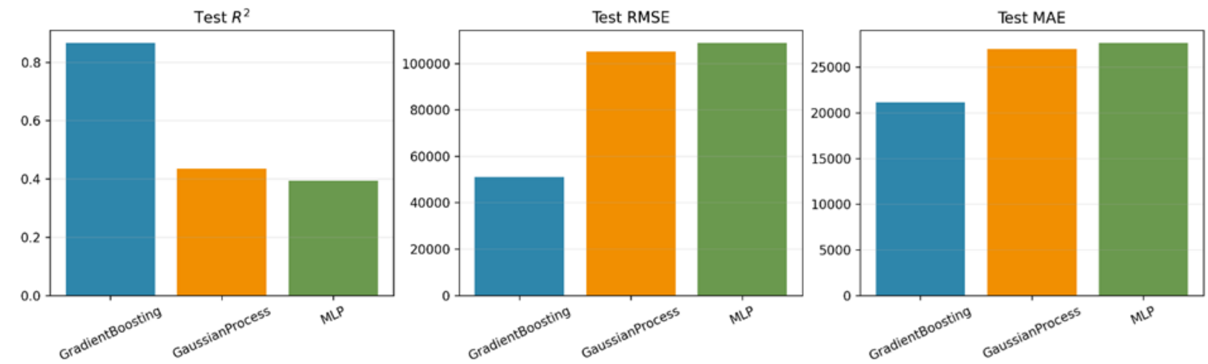

Fig. 7. Test-performance comparison of the machine-learning models

Further evaluation of the prediction accuracy requires analyzing the distribution of model errors across the output spectrum. The corresponding residual distributions for the rotating-frame natural frequency, forward/backward wave frequencies, and critical rotational speed are presented in Figure 8.

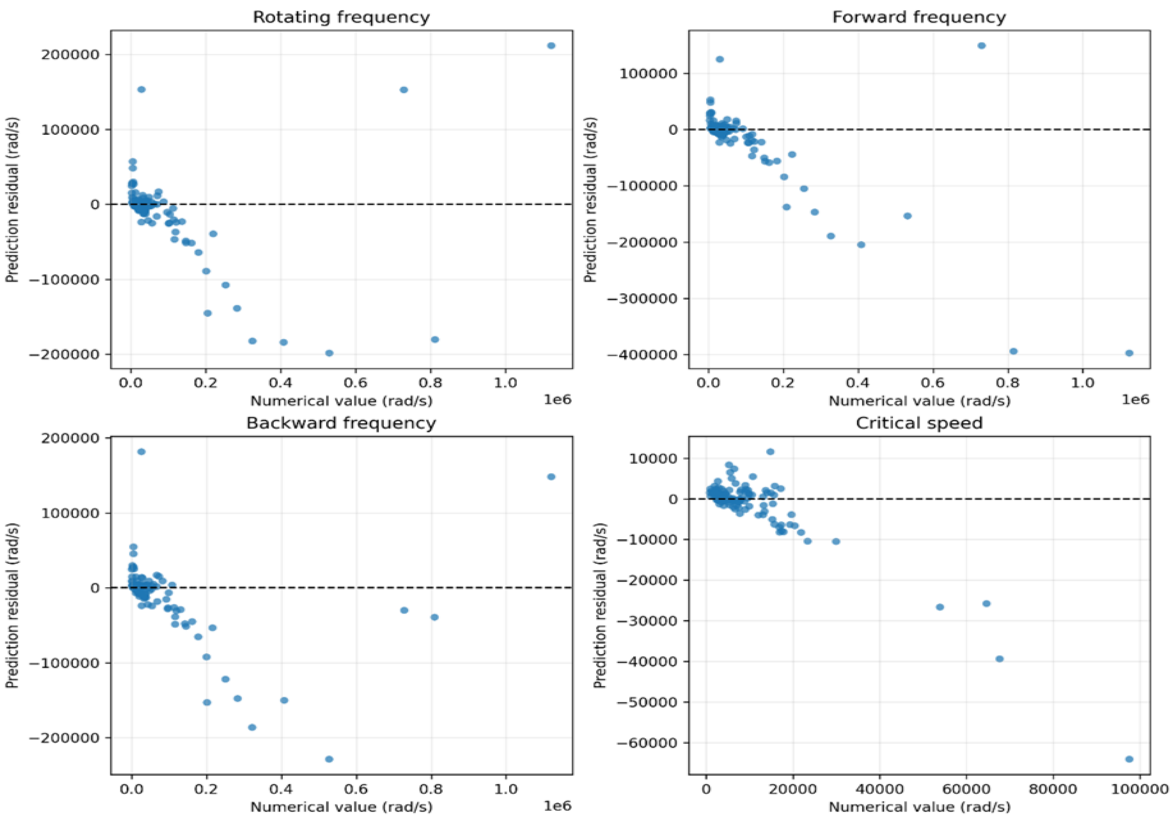

Fig. 8. Prediction residuals for the four response variables

Due to the varying degrees of nonlinearity present in each physical target, model performance differs across individual dynamic variables. The target-dependent coefficient of determination (R^2) values for each candidate surrogate model are compared in Figure 9.

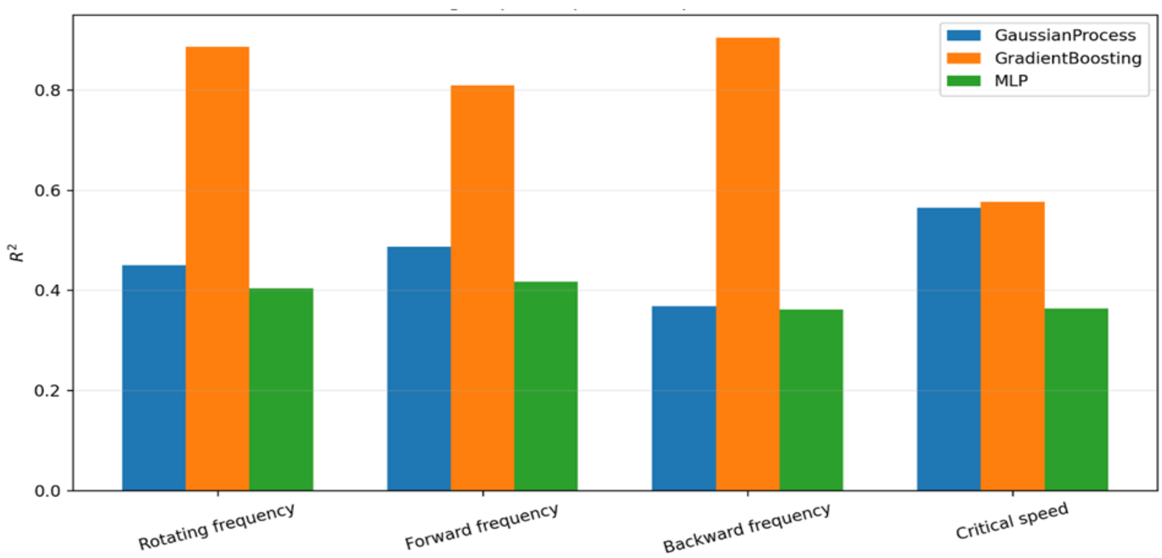

Fig. 9. Target-specific R^2 values of the regression models

The architecture of the multilayer perceptron employed for surrogate prediction is illustrated in Figure 10. The network maps six thermo-mechanical and geometric input parameters to four dynamic response variables through two hidden layers. The overall computational procedure integrating the Chebyshev spectral solution, numerical database generation, machine-learning models, performance evaluation, and prediction stage is summarized in Figure 11.

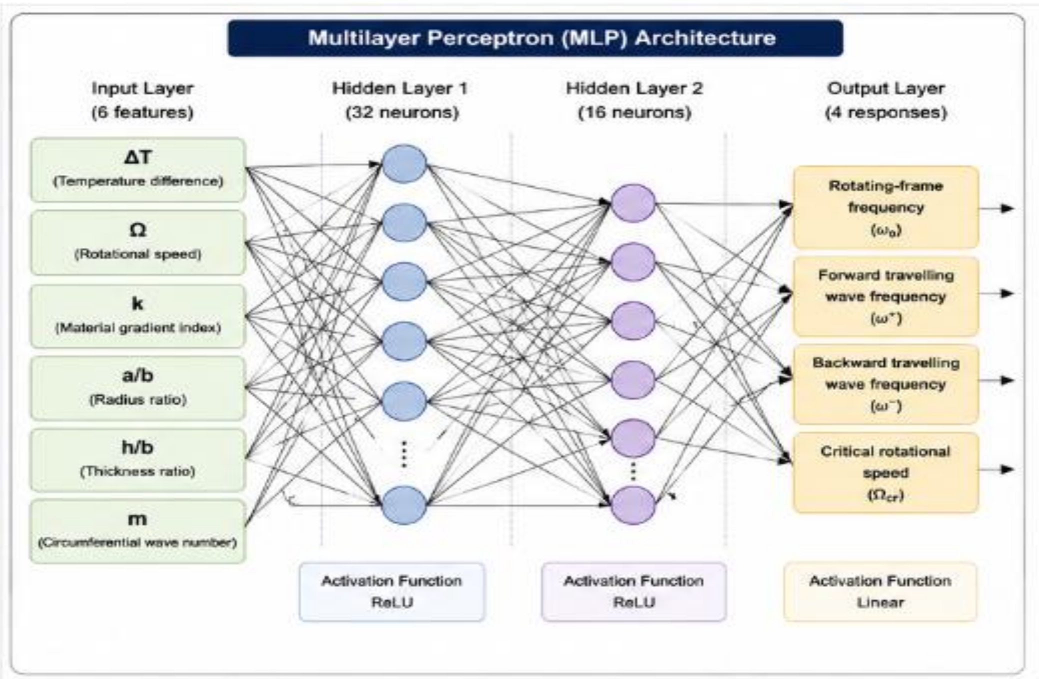

Fig. 10. Multilayer perceptron architecture for prediction of the thermo-vibrational responses and critical rotational speed

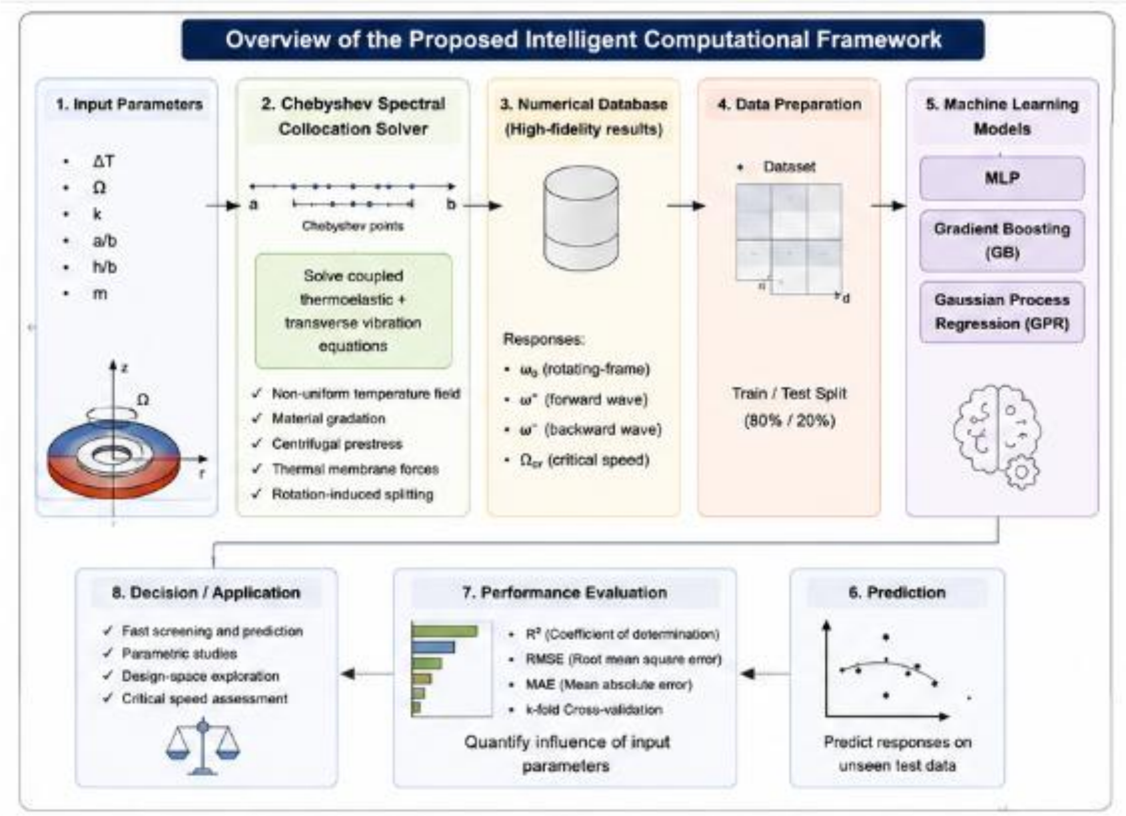

Fig. 11. Intelligent computational framework integrating the Chebyshev spectral solver and machine-learning models for thermo-vibrational prediction

A systematic Chebyshev convergence assessment was conducted by increasing the collocation order from 22 to 46. The first rotating-frame natural frequency changed from 1500.7645 Hz at N = 22 to 1500.2312 Hz at N = 46. The relative difference between the final two discretization levels was only 0.00036%, demonstrating that the spectral solution was effectively independent of the collocation order. The maximum residual associated with the modal quadratic eigenvalue relation was 6.10×10^{-5}, further confirming the numerical consistency of the formulation.

For the baseline disk with a = 50 mm, b = 90 mm, h = 2 mm, n = 1, ΔT = 120 K, Ω = 250 rad/s, and m = 2, the first rotating-frame natural frequency was 1500.23 Hz. The corresponding forward- and backward-travelling wave frequencies were 1579.81 and 1420.65 Hz, respectively. Rotation therefore produced a frequency separation of 159.15 Hz, corresponding to approximately 10.61% of the rotating-frame frequency. The first critical rotational speed was calculated as 9956.52 rad/s. The maximum absolute radial and circumferential prestresses were 72.00 and 150.95 MPa, respectively.

Among the examined surrogate models, Gradient Boosting provided the best overall predictive performance. The target-specific coefficients of determination were 0.8661, 0.8757, and 0.8746 for the rotating-frame, forward-wave, and backward-wave frequencies, respectively. In contrast, critical-speed prediction yielded an R^2 of 0.5770, indicating moderate predictive capability. Consequently, the Gradient Boosting model is suitable for rapid approximation of the modal-frequency responses within the investigated parameter domain, whereas direct Chebyshev spectral calculation remains preferable for reliable critical-speed determination.

The permutation-importance analysis identified the material-gradient index as the dominant input parameter, followed by the radius ratio, thickness ratio, and circumferential wave number. The direct importance of the prescribed temperature difference and the sampled operating speed was comparatively limited within the investigated ranges. This finding indicates that material gradation and disk geometry primarily govern the variation of the combined modal outputs.

5. Conclusions

This study developed a coupled numerical and machine-learning-assisted framework for evaluating the thermal-vibration response and critical speeds of rotating functionally graded Al–SiC annular disks. The Chebyshev spectral collocation solution incorporated radial material gradation, a non-uniform temperature field, temperature-dependent properties, thermo-centrifugal prestress, and rotation-induced travelling-wave splitting within a unified formulation.

For the baseline disk, the first rotating-frame natural frequency was 1500.23 Hz, while the forward- and backward-travelling wave frequencies were 1579.81 and 1420.65 Hz, respectively. The corresponding frequency separation was 159.15 Hz, and the first critical rotational speed was 9956.52 rad/s. Increasing the collocation order from N = 22 to N = 46 reduced the relative change between the final two solutions to 0.00036%, confirming satisfactory numerical convergence.

Among the examined surrogate models, gradient-boosting regression achieved the best overall test performance (R^2 = 0.8661). It predicted the modal-frequency branches with good accuracy; however, its critical-speed prediction was less reliable (R^2 = 0.5770). Therefore, machine learning is suitable for rapid screening within the sampled parameter domain, whereas direct spectral analysis should be retained for critical-speed verification and safety-related design decisions.

The feature-importance results showed that the material-gradient index and geometric ratios were the dominant parameters governing the combined modal response. Overall, the proposed approach provides an efficient basis for the preliminary design and parametric assessment of thermally loaded rotating FGM disks. Future studies should include finite-element or experimental validation, additional boundary conditions, and uncertainty-aware surrogate modeling, particularly for critical-speed prediction.

Acknowledgement

This research was not funded by any grant.

Conflicts of Interest

The authors declare no conflicts of interest.

References

[1] Eraslan, A. N. (2003). Elastic-plastic deformations of rotating variable thickness annular disks with free, pressurized and radially constrained boundary conditions. International Journal of Mechanical Sciences, 45(4), 643–667. https://doi.org/10.1016/S0020-7403(03)00112-7

[2] Nie, G. J., & Batra, R. C. (2010). Stress analysis and material tailoring in isotropic linear thermoelastic incompressible functionally graded rotating disks of variable thickness. Composite Structures, 92(3), 720–729. https://doi.org/10.1016/j.compstruct.2009.08.052

[3] Mahamood, R. M., Akinlabi, E. T., Shukla, M., & Pityana, S. (2012). Functionally graded material: An overview. In Proceedings of the World Congress on Engineering (Vol. III). London, UK. https://hdl.handle.net/10204/8551

[4] Reddy, J. N., & Chin, C. D. (1998). Thermomechanical analysis of functionally graded cylinders and plates. Journal of Thermal Stresses, 21(6), 593–626. https://doi.org/10.1080/01495739808956165

[5] Bayat, M., Saleem, M., Sahari, B. B., Hamouda, A. M. S., & Mahdi, E. (2008). Analysis of functionally graded rotating disks with variable thickness. Mechanics Research Communications, 35(5), 283–309. https://doi.org/10.1016/j.mechrescom.2008.02.007

[6] Asghari, M., & Ghafoori, E. (2010). A three-dimensional elasticity solution for functionally graded rotating disks. Composite Structures, 92(5), 1092–1099. https://doi.org/10.1016/j.compstruct.2009.09.055

[7] Çallıoğlu, H., Bektaş, N. B., & Sayer, M. (2011). Stress analysis of functionally graded rotating discs: Analytical and numerical solutions. Acta Mechanica Sinica, 27(6), 950–955. https://doi.org/10.1007/s10409-011-0499-8

[8] Zafarmand, H., & Hassani, B. (2014). Analysis of two-dimensional functionally graded rotating thick disks with variable thickness. Acta Mechanica, 225(2), 453–464. https://doi.org/10.1007/s00707-013-0966-3

[9] Hassani, A., Hojjati, M. H., Mahdavi, E., Alashti, R. A., & Farrahi, G. (2012). Thermo-mechanical analysis of rotating disks with non-uniform thickness and material properties. International Journal of Pressure Vessels and Piping, 98, 95–101. https://doi.org/10.1016/j.ijpvp.2012.07.010

[10] Jalali, M. H., & Shahriari, B. (2018). Elastic stress analysis of rotating functionally graded annular disk of variable thickness using finite difference method. Mathematical Problems in Engineering, 2018, 1-11. https://doi.org/10.1155/2018/1871674

[11] Hosseini Kordkheili, S. A., & Naghdabadi, R. (2007). Thermoelastic analysis of a functionally graded rotating disk. Composite Structures, 79(4), 508–516. https://doi.org/10.1016/j.compstruct.2006.02.010

[12] Dai, T., & Dai, H. L. (2016). Thermo-elastic analysis of a functionally graded rotating hollow circular disk with variable thickness and angular speed. Applied Mathematical Modelling, 40, 7689–7707. https://doi.org/10.1016/j.apm.2016.03.025

[13] Carrera, E., Entezari, A., Filippi, M., & Kouchakzadeh, M. A. (2016). 3D thermoelastic analysis of rotating disks having arbitrary profile based on a variable kinematic 1D finite element method. Journal of Thermal Stresses, 39(12), 1572–1587. https://doi.org/10.1080/01495739.2016.1207119

[14] Kouchakzadeh, M. A., & Entezari, A. (2015). Analytical solution of classic coupled thermoelasticity problem in a rotating disk. Journal of Thermal Stresses, 38(11), 1267–1289. https://doi.org/10.1080/01495739.2015.1073529

[15] Entezari, A., & Kouchakzadeh, M. A. (2016). Analytical solution of generalized coupled thermoelasticity problem in a rotating disk subjected to thermal and mechanical shock loads. Journal of Thermal Stresses, 39(12), 1588–1609. https://doi.org/10.1080/01495739.2016.1221329

[16] Peng, X. L., & Li, X. F. (2012). Elastic analysis of rotating functionally graded polar orthotropic disks. International Journal of Mechanical Sciences, 60(1), 84–91. https://doi.org/10.1016/j.ijmecsci.2012.04.014

[17] Jalali, M. H., & Jalali, M. R. (2020). Stress analysis of rotating functionally graded polar orthotropic disk under thermomechanical loading. Journal of Vibroengineering, 22(3), 640–656. https://doi.org/10.21595/jve.2019.20575

[18] Afzal, A., & Mujeebu, M. A. (2019). Thermo-mechanical and structural performances of automobile disc brakes: A review of numerical and experimental studies. Archives of Computational Methods in Engineering, 26(5), 1489–1513. https://doi.org/10.1007/s11831-018-9279-y

[19] Belhocine, A., & Bouchetara, M. (2013). Investigation of temperature and thermal stress in ventilated disc brake based on 3D thermomechanical coupling model. Ain Shams Engineering Journal, 4(3), 475–483. https://doi.org/10.1016/j.asej.2012.08.005

[20] Jiregna, I. T., & Lemu, H. G. (2021). Thermal stress analysis of disc brake using analytical and numerical methods. IOP Conference Series: Materials Science and Engineering, 1201(1), Article 012033. https://doi.org/10.1088/1757-899X/1201/1/012033

[21] Farooq, D., Moslem, S., Hussan, S., Riaz, M. A., Esztergár-Kiss, D., & Martinez-Pastor, B. (2026). Spherical fuzzy analytic hierarchy process approach to evaluate the effect of significant factors on drivers' perceived risk related to road safety: A case study. Discover Civil Engineering, 3(1), Article 167. https://doi.org/10.1007/s44290-026-00557-0

[22] Kayiran, H. F. (2026a). Sustainable engineering design: Accelerating thermoelastic stress prediction in hybrid SiC–Ti6Al4V components via machine learning. International Journal of Sustainable Development Goals, 2, 655–667. https://doi.org/10.59543/dbs4d790

[23] Kayiran, H. F. (2026b). Explainable physics-informed deep learning framework for thermoelastic analysis of rotating Ti-6Al-4V disks. Applied Expert Systems and Knowledge Management, 1, 1–15. https://doi.org/10.59543/qhn3ek50

[24] Kayiran, F. (2026c). Physics-informed machine learning for predicting thermomechanical stress in rotating carbon-aramid hybrid composites. Knowledge and Decision Systems with Applications, 2, 408–421. https://doi.org/10.59543/rpwq1n92

[25] Shen, H.-S. (2009). Functionally graded materials: Nonlinear analysis of plates and shells. CRC Press. https://doi.org/10.1201/9781420092578

[26] Timoshenko, S. P., & Goodier, J. N. (1970). Theory of elasticity (3rd ed.). McGraw-Hill.

[27] Trefethen, L. N. (2000). Spectral methods in MATLAB. Society for Industrial and Applied Mathematics. https://doi.org/10.1137/1.9780898719598

[28] Bishop, C. M. (2006). Pattern recognition and machine learning. Springer.
[29] Friedman, J. H. (2001). Greedy function approximation: A gradient boosting machine. The Annals of Statistics, 29(5), 1189–1232. https://doi.org/10.1214/aos/1013203451
[30] Rasmussen, C. E., & Williams, C. K. I. (2006). Gaussian processes for machine learning. MIT Press. https://doi.org/10.7551/mitpress/3206.001.0001